Initiation of T cell signaling by CD45 segregation at 'close-contacts'

Veronica T Chang[1]*, Ricardo A Fernandes[1]*, Kristina A Ganzinger[2]*, Steven F Lee[2]*, Christian Siebold[3], James McColl[2], Peter Jönsson[2], Matthieu Palayret[2], Karl Harlos[3], Charlotte H Coles[3], E Yvonne Jones[3], Yuan Lui[1], Elizabeth Huang[1], Robert J C Gilbert[3], David Klenerman[2§], A Radu Aricescu[3§] & Simon J Davis[1§]

* These authors contributed equally to the work

§ Correspondence: simon.davis@imm.ox.ac.uk, radu@strubi.ox.ac.uk, dk10012@cam.ac.uk

[1] Radcliffe Department of Medicine and MRC Human Immunology Unit,
John Radcliffe Hospital,
University of Oxford,
Oxford OX3 9DS,
United Kingdom

[2] Department of Chemistry,
University of Cambridge,
Cambridge,
CB2 1EW

[3] Division of Structural Biology,
Wellcome Trust Centre for Human Genetics,
University of Oxford,
Oxford OX3 7BN
(present address for V.T.C.)

Abstract

It has been proposed that the local segregation of kinases and the tyrosine phosphatase CD45 underpins T cell receptor (TCR) triggering, but how segregation would occur and whether it can initiate signaling is unclear. Using structural and biophysical analysis we show that the extracellular region of CD45 is rigid and extends beyond the distance spanned by TCR-ligand complexes, implying that sites of TCR-ligand engagement would sterically exclude CD45. We also show that the formation of new structures characterized by spontaneous sub-micron scale CD45 and kinase segregation, called 'close-contacts', initiates signaling even when TCR ligands are absent. Our work reveals the structural basis for, and the unexpectedly potent signaling effects of local CD45 and kinase segregation. TCR ligands could heighten signaling simply by holding receptors in close-contacts.

Introduction

It is known that the binding of foreign antigens presented by major histocompatibility proteins results in T cell receptor (TCR) phosphorylation by the tyrosine kinase, Lck, but not how[1]. An important clue is that T cells express unusually large amounts of a receptor-type protein tyrosine phosphatase (RPTP), CD45, on their surfaces[2]. Owing to its abundance (>100,000 molecules/cell and >3 molecules/TCR[3]) and its high specific activity (10-1000 fold higher than that of kinases[4]) CD45 likely constrains tyrosine phosphorylation in resting cells. However, T cells lacking CD45 cannot be activated[5], implicating it also in the initiation of signaling. This is at least partly explained by CD45 being required to activate Lck by dephosphorylating an inhibitory tyrosine at the C-terminus of the kinase[2].

A second important observation is that interventions acting globally to block phosphatases or activate kinases induce spontaneous T cell activation[6,7]. The kinetic-segregation (KS) model[8,9] was proposed to explain how similar changes in kinase and/or phosphatase activity might be invoked. The KS model incorporated the observation[10] that, owing to their large size, glycocalyx components such as CD45 will likely be excluded from sites of TCR-ligand engagement. The KS model postulates that low amounts of TCR phosphorylation are maintained by an equilibrium between kinases and CD45, until it is disturbed locally in favor of the kinases when CD45 is sterically excluded from hypothetical structures called 'close-contact zones' where TCRs and other small proteins such as CD2 engage their ligands,

resulting in net receptor phosphorylation[8,9]. However, segregation needs to occur over short length scales (likely <1 μm[11]) to allow ligand discrimination.

Although it has substantial experimental support[1,9], several key elements of the KS model are unverified. First, signaling-coincident close-contact zone formation characterized by local CD45 and kinase segregation has gone unreported. TCR microclusters exclude CD45 (ref 12) but these structures are distinct from close-contact zones predicted by the KS model to form TCR independently. There is also large-scale CD45 exclusion during immunological synapse formation[13,14] but this is too late to impact early signaling[15]. Second, the mechanism of CD45-kinase segregation, if it occurs, is not fully explained owing to uncertainty about the structural properties and dimensions of the extracellular region of CD45[16]. Third, it is unclear whether CD45 and kinase segregation could effect receptor triggering. CD45 blocks signaling if it can access TCR-ligand complexes[17-19] but this confirms only that CD45-kinase segregation is required for signaling, not that it is sufficient. Fourth, as has been suggested[20], CD45 exclusion could prevent rather than initiate signaling because it is needed to activate Lck[2]. However, CD45 is remarkably unspecific[21] and the TCR is an even better substrate than Lck[22], suggesting overall that CD45 exclusion could favor TCR phosphorylation. Finally, whether receptor triggering relies on ligand-induced effects such as receptor oligomerization or conformational changes rather than ligand engagement only, is unresolved[1]. However, the prediction that signaling would occur ligand independently if, e.g., phosphatase-excluding close-contact zones formed that were so large that kinase activity was effectively unopposed, offers a way to discriminate between the KS model and other, more ligand-centric explanations of receptor triggering.

In this study we show that the extracellular domain (ECD) of CD45 is rigid and extends beyond the distance spanned by TCR-ligand complexes, explaining why it will be excluded from sites of TCR-ligand engagement. Live-cell imaging reveals the formation of sub-micron scale structures exhibiting several of the properties of close-contact zones postulated by the KS model. The formation of these structures, which we call 'close-contacts' is capable of initiating signaling even when TCR ligands are absent. Together these findings identify the structural basis for, and the unexpectedly potent signaling effects of local CD45-kinase segregation.

Results

Structure of the modular region of the CD45 ECD

CD45 is expressed as multiple isoforms according to cell type, developmental stage and cell activation state[2]. The CD45 ECD was predicted[16] to comprise an N-terminal mucin-like segment followed by a 'cysteine-rich' domain (d1) and three fibronectin type 3 (FN3) domains (d2-d4). Human CD45 isoforms arise from alternative splicing of exons 4, 5 and 6 of the *PRPTC* gene, which alters the length of the mucin-like segment. The smallest (CD45R0) and longest (CD45RABC) isoforms are encoded by transcripts lacking or comprising all the alternatively spliced sequence and have mucin-like segments of 41 and 202 residues, respectively (**Fig. 1a**). We expressed in mammalian cells the intact ECDs of human CD45R0 and CD45RABC along with d1d2, d1-d3 and d1-d4, and rat (r) CD45 d3d4 (**Fig. 1a** and **Supplementary Fig. 1a**). Multi-angle light scattering (MALS) analysis indicated that CD45d1-d4 and the CD45R0 and CD45RABC ECDs are monomeric in solution (at concentrations of ~10 μM; **Fig. 1b**). We determined the crystal structures of the CD45d1-d4 segment (to 2.9 Å resolution), CD45d1-d3 (3.1 Å resolution), CD45d1d2 (2.7 Å resolution) and rCD45d3d4 (2.8 Å resolution; see **Supplementary Figures 1b-d** for representative electron density and **Supplementary Table 1** for crystallographic data). CD45d1-d4 (**Fig. 1c**) comprises a 'beads on a string' array of four modular domains stabilized by eight disulfide bonds, seven forming part of the core of each domain and one at the d1:d2 interface (**Fig. 1d**). Inspection of the lattice did not reveal any potentially important oligomerization interfaces consistent with the MALS data and with CD45 diffusing as monomers at the T cell surface[23].

Domain 1 as well as domains 2-4 have elements of the FN3 fold (**Fig. 1e**). Structural comparisons using DALI (www.ekhidna.biocenter.helsinki.fi/dali_server) revealed that d3 and d4 are classical FN3 domains [best hits: r.m.s.d. of 1.9 Å for 91 Cα positions of d3 and the fifth FN3 domain of NEO1 (pdb 4BQB); and r.m.s.d. of 1.7 Å for 87 Cα positions of d4 and the third FN3 domain of Tenascin (pdb 1TEN)]. D1 and d2, however, exhibit degenerate topology unprecedented among FN3 family structures. The absence (in d1) or rearrangement (in d2) of β-strands β3 and β4 results in splaying apart of one edge of the typical FN3 β-sandwich (**Fig. 1e**). In d1 a disulfide bond (numbered II in **Fig. 1d**,**e**) and deletion of a residue orientate this region away from the β-sheet (**Fig. 1e**, top left panel). A

similar effect is achieved in d2 where disulfide bridge V forms a novel connection between β-strands β3 and β6. Although the d1 sequences of CD45 orthologs could only be tentatively aligned, d1 of jawed fish seemed substantially longer than that in hagfish or mammal CD45 (data not shown), implying that this has been a region of considerable structural plasticity.

Only six of ten predicted N-linked glycosylation sites in CD45d1-d4 could be modeled as N-acetylglucosamine moieties left by pre-crystallization deglycosylation (**Fig. 1c**). Most predicted N-linked glycosylation sites are located in d1 of CD45 (**Fig. 1f**) and mapping of all these sites in mammals (**Supplementary Fig. 2a**) revealed that most are poorly conserved and that domains 1 and 2 are usually more heavily glycosylated than domains 3 and 4. One side of the domain 3 and 4 segment is largely free of glycosylation and substantially less charged than the opposite side (**Supplementary Fig. 2b**), perhaps facilitating access to substrates with small ECDs, such as TCR-CD3 complexes (**Supplementary Fig. 2c**).

The CD45 d1-d4 segment is rigid

The two CD45d1-d4 copies comprising the asymmetric unit were essentially identical with an r.m.s.d. of 1.5 Å for 346 Cα positions, suggesting that CD45d1-d4 is rigid. Inspection of the shorter CD45 constructs from five different crystal environments (**Supplementary Table 1**) supported this since there was less than 5° of rotational freedom between each domain pair (**Fig. 2a**). The domains are connected by very short and, for the d1-d2 and d3-d4 interfaces, proline-rich linkers allowing extensive inter-domain interactions (average surface area buried is 345 $Å^2$ versus 257 $Å^2$ for RPTPμ[24]; **Fig. 2b**-**d**). The d1-d2 interface is mainly hydrophobic with phenylalanine and tyrosine side-chains clustered at its center (Y237 and F246 from d1 and F329, Y371 and F376 from d2; **Fig. 2b**). This arrangement is stabilized by a salt-bridge formed by E273 and K303 at the interface edge and by a centrally-positioned disulfide bond between C274 and C331 (numbered III in **Fig. 1d**). In contrast, a centrally-located arginine (R467 from d3) forming a network of hydrogen bonds and a salt-bridge with d2 residues stabilizes the d2-d3 interface (**Fig. 2c**). The d3-d4 interface is dominated by a hydrophobic stacking interaction between Y450 of d3 and P512 of d4 supported by hydrogen bonding between the main chain oxygen of N510 and main chain nitrogen of A481 (**Fig. 2d**).

Sequence conservation in the mammalian CD45 ECD is extremely low (<15% identity), contrasting with the high levels (>90%) in, e.g., type II RPTP ECDs[24]. No conserved d1-d4 surfaces are likely to bind ligands, and what limited conservation there is (**Fig. 2e**) mostly maps to the three domain interfaces suggesting that ECD rigidity is characteristic of CD45. However, conserved networks of residues also cap the ends of the d1-d4 segment (**Fig. 2e** and **Supplementary Fig. 2d,e**). Hydrophobic interactions involving I233, V252, L250, V256 and I281, along with a conserved disulfide (C226-C286) and H-bonding of K229 and Y230 with E254 might help position the mucin-like extension at the d1-d4 N-terminus (**Supplementary Fig. 2d**). Similarly, a hydrophobic core comprising V491, M499, V501, L518, V520, F537, L542 and F550, and H-bonds between Q543-Y548, T546-T570 and S495-S498 rigidify the base of the molecule, stabilizing D496 and creating a conserved negatively-charged surface perhaps influencing ECD orientation at the cell surface (**Supplementary Fig. 2e**). A final notable feature is that whereas FN3 domains often lack cysteines, domains 1-3 of CD45 from a variety of species contain 3-5 cysteines/domain on average (range 0-7), which are generally conserved among mammalian orthologs but not across phyla. Assuming they form disulfides the accumulated cysteines would also rigidify the CD45 ECD.

Axial dimensions of the CD45 ECD

The structural analysis was extended using single-particle negative staining electron microscopy (EM; **Supplementary Fig. 3a**). To aid visualization the intact CD45R0 ECD was fused with the globular ~70kD ECD of semaphorin 6a (Sema6A; pdb 30KW; **Fig. 3a**). Class averages (**Fig. 3b** and **Supplementary Fig. 3b**) resolved the FN3 domain array and Sema6A, with linking density corresponding to the mucin-like segment. A 3D reconstruction of the data to 33 Å resolution could be directly fitted with the d1-d4 and Sema6A crystal structures but the mucin segment was not resolvable owing to limited map resolution (**Fig. 3c** and **Supplementary Fig. 3c**-**e**). Because Sema6A was positioned consistently enough for reconstruction, however, these data indicate that the 41 residue mucin-like region is rigid, as expected for mucin-like structures of this length[25]. The length of the mucin-like segment, ~80 Å, is compact versus typical mucins (~2.5 Å/residue[25]) but similar to CD43 (~2 Å/residue[26]). At ~216 Å from N- to C-terminus the CD45R0 ECD is smaller than suggested by rotary-shadowing experiments[27] but matches predictions based on domain

assignments[16]. Sema6A-CD45RABC failed to bind carbon-coated EM grids and was not analyzed.

To investigate whether CD45 will segregate from sites of TCR-ligand engagement because it is likely 'upright' at the cell surface we tested whether the CD45 ECD lies prone or projects away from supported lipid bilayers (SLBs) using variable-angle total internal reflection fluorescence microscopy (VA-TIRFM)[28] (**Fig. 3d**), which discriminates between the mean axial positions of fluorophores above a surface. We placed fluorescent tags at their N-termini and recorded the integrated fluorescence from CD45 ECDs anchored to SLBs as a function of incident angle, normalized against that of a labeled lipid in adjacent SLBs (**Fig. 3d**). The different slopes obtained could be attributed to differences in the axial height of the proteins, with the mean label position of the RABC and R0 isoforms experiencing significantly different evanescent fields versus d1-d4, whose dimensions are comparable to TCR-peptide-MHC II-CD4 and CD2-LFA-3 complexes (**Fig. 3e**). The scale of the differences in slope (>1.6-fold) correlated with the structural data, strengthening the hypothesis that in order to maximize the entropy of the ECD-SLB system wherein the ECDs were flexibly linked to the SLB, the ECDs were on average upright, with CD45RABC and CD45R0 extending significantly beyond the distance spanned by TCR-ligand complexes.

Signaling at 'close-contacts' driven by CD45 segregation

The structural data implied that the mechanical properties of the CD45 ECD are important for its function, consistent with the ECD driving CD45 from sites of TCR-ligand engagement. However, CD45-kinase segregation has only been observed during synapse formation, too late to affect TCR triggering[15]. We therefore characterized CD45 organization at very early stages of T cell contact formation and tested whether ECD-dependent CD45-Lck segregation coincides with, and is required for, TCR signaling.

CD45 organization on live Jurkat T cells was studied with TIRFM using fluorescent anti-CD45 Fab fragments to label the phosphatase. High cell activity (i.e. surface and/or shape changes) at 37°C necessitated data collection at 20°C. Resting Jurkat T cells first placed on glass coverslips coated with non-activating antibody (bovine IgG), formed multi-focal contacts with the surface. Rather than being homogeneously distributed CD45 was

spontaneously excluded at each point of contact, forming ring-like arrangements (**Fig. 4a**). The contacts expanded to diameters >1 μm in ~200 s (**Fig. 4a**), relied on close membrane-surface apposition (**Fig. 4b**), labelled strongly for actin (**Fig. 4c**) and formed actin-dependently (**Fig. 4d**). TCR-lacking J.RT3-T3.5 cells also formed contacts (**Fig. 4c**), indicating that contact formation was TCR independent. The phosphatase was sterically excluded since CD45 with an ECD comprised of a nine-residue haemagglutinin tag (HA-CD45) entered the contacts (**Fig. 4e**). Importantly, a fluorescent non CD4-binding mutant of Lck (mLck) was not excluded (**Fig. 4f**), indicating that formation of the contacts results in spontaneous local kinase-phosphatase segregation. Primary T cells formed similar contacts (**Fig. 4g**), as did T cells interacting with glass surfaces coated with activating anti-CD3ε antibody (OKT3; **Supplementary Fig. 4a**). Given their similarity to 'close-contact zones' invoked by the KS model[8,9], we call these structures 'close-contacts'. Unexpectedly, whereas non-lymphoid e.g. human embryonic kidney cells formed sinuous contacts with glass substrates (**Fig. 4h**), they formed robust T cell-like close-contacts upon expressing a glycocalyx comprised of CD45RABC lacking a cytoplasmic domain (**Fig. 4i**).

To test whether CD45-Lck segregation observed at close-contacts coincides with and is required for signaling, we engineered forms of mLck that would leave close-contacts with CD45 (**Fig. 5a,b**) and tested their ability to reconstitute TCR signaling in Lck-deficient J.CaM1.6 cells contacting OKT3-coated surfaces. At the time of calcium signaling under these conditions (~2 min; **Supplementary Fig. 4b**), a fluorescent membrane-spanning form of mLck, TMLck, was not excluded from close-contacts formed with the OKT3-coated surface (**Fig. 5c**, left *panel*), producing anti-correlated fluorescence line profiles versus CD45 (**Fig. 5c**, right *panel*). Attaching the CD45R0 ECD to TMLck, however, dramatically altered the distribution of the kinase following surface contact (**Fig. 5d**). Overall, the contacts could be divided into two classes corresponding to patterns formed by 'short-form' Lck (mLck and TMLck) and 'long-form' Lck (RABCLck, R0Lck and d1-d4Lck; **Supplementary Fig. 4a,c-f**; **Supplementary Table 2**). Whereas short-form Lck proteins and CD45 gave poorly correlated signals (**Fig. 5e** and **Supplementary Fig. 5a**) the spatial distributions of CD45 and the long-forms were well correlated (**Fig. 5f** and **Supplementary Fig. 5b**; **Supplementary Table 2**). ECD size and signaling were also strongly correlated (**Fig. 5g** and **Supplementary Videos 1,2**). OKT3 induced calcium responses in >50% of J.CaM1.6

cells expressing TMLck upon contact whereas significantly fewer cells expressing RABCLck, R0Lck and d1-d4Lck responded (<30%), and these responses were not significantly different from those of J.CaM1.6 cells. The dependence of signaling on Lck dimensions, also observed at 37°C (**Supplementary Fig. 4g**) revealed that receptor triggering requires the CD45 ECD-dependent segregation of the phosphatase and Lck at close-contacts.

Ligand-independent TCR triggering at close-contacts

The finding that CD45 and Lck spontaneously segregate on bovine IgG-coated glass surfaces offered a test of whether CD45-kinase segregation is sufficient to effect TCR triggering, which discriminates between the KS model and strictly ligand-dependent explanations of receptor triggering. At 37°C, IgG-coated surfaces induced calcium signaling by primary $CD4^+$ and Jurkat T cells (49% and 68% activated cells, respectively; **Supplementary Fig. 4h**). These responses were comparable to those induced by OKT3 (83% and 90% respectively; **Supplementary Fig. 4h-j)**. TCR-lacking J.RT3-T3.5 cells were less responsive indicating that local CD45-Lck segregation initiates TCR-dependent, ligand-independent signaling. Using SLBs to approximate native cell-cell interactions, we next investigated whether CD45-Lck segregation resulted in TCR triggering *per se*, i.e. receptor phosphorylation.

T cell-SLB contact was initiated by inserting the small adhesion protein rat CD2 into SLBs at physiological densities (100-300 molecules/μm^2) and by using Jurkat T cells expressing a non-signaling T92A mutated form of CD48 that binds rat CD2 with an affinity similar to that of human CD2-CD58 interactions (~20 μM)[29]. Contacts formed rapidly and were characterized by the accumulation of fluorescently labeled CD2 under the cell and, invariably, CD45 exclusion (**Fig. 6a**, **Supplementary Fig. 6a and Supplementary Video 3**). Typical contacts (**Fig. 6a**, *top*) reached 1-3 μm in diameter in 10s and expanded to 8-12 μm within 3-5 min. Occasionally, multi-focal contacts also formed (**Fig. 6a**, *bottom*). CD45 exclusion was dependent on CD2-CD48 binding (**Supplementary Video 4**) and independent of the fluorescent labels used (**Supplementary Fig. 6b**). However, neither CD45 lacking its ECD (HA-CD45; **Fig. 6b** and **Supplementary Fig. 6c**), nor the TCR (**Fig. 6c** and **Supplementary Fig. 6d**) nor mLck (**Fig. 6d**, **Supplementary Fig. 6e,f and Supplementary Video 3**) were excluded from the contacts. The extent of CD45-Lck segregation was quantified ~10' after contact formation (**Fig. 6e**). Assuming copy numbers

of ~200,000 for CD45 (ref. 3) and 40,000 for mLck[30] the CD45:Lck ratio decreased from 5:1 in resting cells to 2.3:1 at the T cell-SLB contacts.

The change in CD45:mLck ratio upon T cell-SLB contact was accompanied by calcium signaling (**Fig. 6f**) at levels approaching those induced by immobilized OKT3 (typically 80-90% responses; **Supplementary Fig. 4g**). The response was significantly reduced by truncated CD45 (HA-CD45) as observed for direct TCR stimulation[17] (**Fig. 6f**). Jurkat T cells expressing CD48 but lacking TCRs, Lck or Zap70 were also less- or unresponsive (**Fig. 6f**). Within two minutes of CD48-expressing Jurkat T cells interacting with SLBs containing slightly higher levels of CD2 (~1000 molecules/μm^2), small clusters of fluorescently labeled Zap70 molecules accumulated at the cell-SLB contact (**Fig. 7a** and **Supplementary Video 5**). Significantly fewer clusters accumulated in TCR-deficient cells (**Fig. 7b,c** and **Supplementary Video 6**) although they appeared at similar times (data not shown). The fluorescence intensities of the Zap70 clusters (i.e. their size) were greater in Jurkats than in TCR-deficient cells (**Fig. 7d**) and the cluster intensities increased during the first 180 seconds of contact (**Fig. 7e**). Since Zap70 recruitment depends strictly upon TCR phosphorylation these findings indicate that the TCR is triggered on the SLBs in a contact- and Lck-dependent but ligand independent manner. Finally, in contrast to SLBs containing TCR ligands (e.g. ref. 31), Zap70 cluster movement was not centripetal (**Supplementary Fig. 7**) suggesting that immunological synapse formation is not mobilized under these conditions. The sequence of events proposed to result in ligand-independent TCR triggering are illustrated in **Supplementary Video 7**.

Discussion

To better understand how CD45 might influence receptor triggering we determined the structure of its extracellular region. The relationship between the structure and function of the ECD of CD45 is illuminated by comparisons with those of RPTPμ and RPTPσ, two large type II RPTPs[24,32]. The organization and dimensions of the rigidly arranged FN3 domains of CD45 are comparable to those in RPTPμ but the domain interfaces are larger and the d1 and d2 topologies unique. In highly flexible RPTPσ the domain interfaces are generally small or non-existent. The degree of CD45 sequence conservation is very low compared to RPTPμ. The only conservation beyond that required for FN3 domain integrity is at domain interfaces

influencing ECD shape and rigidity, at the top of the d1-d4 segment perhaps affecting positioning of the mucin-like segment and at the base, possibly influencing interactions with the membrane. The CD45 ECD is also richer in cysteines likely to rigidify the protein than all other FN3-like domain-containing proteins including RPTPμ and RPTPσ. Overall, it seems that it is the mechanical properties of the ECD that are most important to the functioning of CD45. The apparently rigid mucin-like segment of CD45R0 extends the molecule to 216Å. Assuming that the dimensions of TCR-ligand complexes are comparable to those determined crystallographically (~150Å)[33,34], even the smallest CD45 isoform will be sterically excluded from sites of TCR-ligand engagement if CD45 stands upright, as our VA-TIRF experiments suggest. Otherwise the presence of CD45 would deform the lipid membranes in the contact region, increasing the energy of the system as discussed elsewhere.[35]

We also show that at regions of contact with artificial and model cell surfaces, T cells form previously undescribed structures we call 'close-contacts' characterized by ECD-dependent CD45 exclusion. To routinely observe multifocal close-contacts on glass substrates it was necessary to image at 20°C. These structures may have gone undetected previously because they are generally short-lived at 37°C and more difficult to observe with the higher activity cells exhibit at this temperature. At the time of signaling initiated by antibodies on these surfaces the close-contacts had diameters < 1μm. In bilayers at 37°C, mostly single large close-contacts formed quickly in the presence of CD2 and CD48, suggesting that CD45 is passively excluded from any site where CD2-ligand sized complexes assemble, including TCR-ligand complexes[36]. Close-contacts formed on bilayers are therefore qualitatively similar to close-contact zones invoked by the KS model[8,9]. Close-contacts observed on glass surfaces are distinct from CD45-excluding TCR microclusters because they form TCR-independently, vary in size and do not move centripetally[31]. The larger contacts formed on bilayers differ from CD45-excluding immunological synapses because they form within a minute rather than 15-30 minutes (see e.g. ref 31), and do not centrally accumulate TCRs. The processes driving initial close-contact formation very likely correspond to F actin-rich pseudopods[37]. Surprisingly, non-lymphoid cells formed T cell-like close-contacts upon expressing a single glycocalyx component, i.e. cytoplasmic domain-lacking CD45, suggesting that the appearance of a CD45-containing glycocalyx on primitive lymphoid cells

during their evolution could have allowed their utilization of contact-sensitive, molecular segregation-based receptor signaling.

Spontaneous CD45 and kinase segregation at close-contacts coincided with strong ligand-independent, TCR-dependent signaling, revealing the extent to which CD45 and kinase segregation *per se* can effect receptor triggering. The Lck:CD45 ratio measured in close-contacts formed on SLBs (~50%) is similar to that giving half-maximal phosphorylation of CD3 by Lck and CD45 attached to lipid bilayers (68%)[22]. This suggests that the ratio of Lck:CD45 activities in resting cells might be set at a level that ensures TCR phosphorylation is sensitive to local CD45 segregation. Global alterations in this ratio, achieved pharmacologically or with genetic interventions initiate spontaneous ligand-independent signaling in T cells[6,7], and our work identifies a physiological counterpart for these effects. Because it can be triggered in the absence of ligands, the TCR cannot be strictly dependent on ligand-induced receptor oligomerization and/or conformational changes. It is also unlikely to depend on physical forces acting through it[38] because, in our bilayer experiments, the receptor was triggered by CD45 and kinase segregation even while suspended between the T cell surface and the SLB by CD2 and CD48. The ability of the TCR to be triggered in this way blurs the distinction between receptors and adaptors or signaling hubs such as LAT that lack ECDs but are heavily phosphorylated during T cell activation. Another example is CD6, which functions as both receptor and signaling hub[39].

What safeguards T cells from signaling at close-contacts when TCR ligands are absent? Close-contacts formed *in vivo* are likely smaller and shorter-lived than those formed in the absence of the glycocalyx of antigen-presenting cells in our experiments, perhaps allowing at most only sub-threshold signaling in the absence of TCR ligands. Moreover, without TCR ligands co-receptor engagement is impossible, also constraining signaling. However, TCR triggering in close-contacts lacking ligands might nevertheless be important in certain circumstances, e.g. during β-selection when the TCR has to signal from the cell surface in a partially assembled form (the preTCR), and does so even after its extracellular domains have been removed[40]. Conceivably, the threshold for TCR activation is fine-tuned by variation in the CD45 ECD during T cell development and differentiation.

In conclusion, we have shown that CD45 spontaneously segregates from Lck when T cells interact with lipid bilayers and the inter-surface distance is set by complexes of adhesion proteins (CD2 and CD48) whose dimensions are comparable to those of TCR-ligand complexes[36]. We showed that the exclusion of CD45 at the close-contacts is explained by differences in the dimensions of CD45 and these complexes, and demonstrated that this suffices to trigger the TCR and initiate signaling, even when TCR ligands are absent. As we have proposed[8,9], at similar but smaller or more dynamic close-contacts formed *in vivo* that would otherwise sustain tonic or sub-threshold signaling at best, TCR ligands might increase the probability of signaling simply by holding the receptor in the close-contacts where encounters with Lck are favored over those with CD45.

Acknowledgements

The authors thank R.A. Cornall, M.L. Dustin and P.A. van der Merwe for comments on the manuscript and S. Ikemizu for useful discussions about the structure. We also thank W. Lu and T. Walter for technical support with protein expression and crystallization, staff at Diamond Light Source beamlines I02, I03 and I04-1 (proposal mx10627) and European Synchrotron Radiation Facility beamlines ID23EH1 and ID23EH2 for assistance at the synchrotron, G. Sutton for assistance with MALS experiments, and M. Fritzsche for advice on the calcium analysis. This work was funded by the Wellcome Trust, the UK Medical Research Council, the UK Biotechnology and Biological Sciences Research Council and Cancer Research UK. The Oxford Division of Structural Biology is part of the Wellcome Trust Centre for Human Genetics, Wellcome Trust Core Award Grant Number 090532/Z/09/Z. We acknowledge financial support from INSTRUCT (http://www.structuralbiology.eu/). The OPIC electron microscopy facility was funded by a Wellcome Trust JIF award (060208/Z/00/Z).

COMPETING FINANCIAL INTERESTS

The authors declare no competing financial interests.

Accession codes

Structure co-ordinates have been assigned identifiers 5fmv (CD45d1-d4), 5fn6 (hCD45d1-d3) 5fn7 (hCD45d1-d2), and 5fn8 (rCD45d3-d4) at the Protein Data Bank.

Author contributions

V.T.C., R.A.F., K.A.G., S.F.L., E.Y.J., R.J.C.G., D.K., A.R.A. and S.J.D. designed experiments; V.T.C., R.A.F., K.A.G., S.F.L., J.McC., P.J., M.P., K.H., C.S., C.H.C., Y.L., E.H., R.J.C.G. and A.R.A. performed experiments; R.A.F., K.A.G., S.F.L., C.S., E.Y.J., R.J.C.G., V.T.C., A.R.A., D.K. and S.J.D. drafted and/or edited the manuscript.

Figures

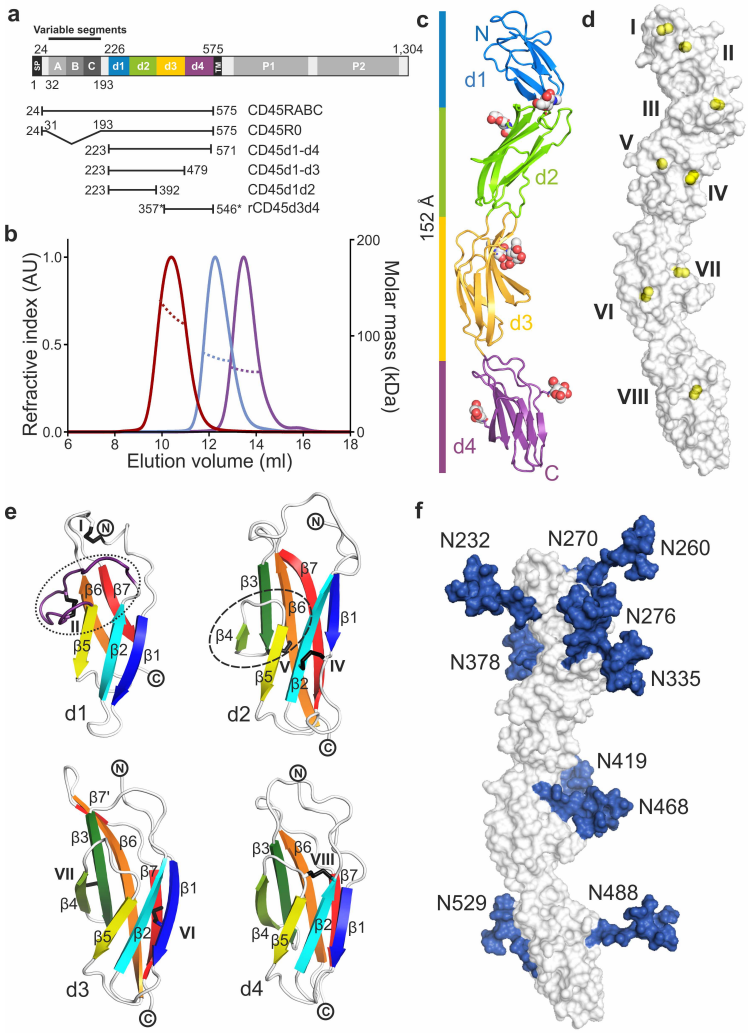

Figure 1

Crystal structure of the human CD45 ECD d1-d4 segment. (**a**) Schematic representation of the full-length human CD45 sequence. SP, secretion signal peptide; TM, transmembrane domain; P1 and P2, tyrosine-protein phosphatase catalytic domains. A, B and C indicate exons spliced out in the R0 isoform. Domains observed in the crystal structures are colored blue (d1), green (d2), orange (d3) and purple (d4). Constructs used for functional studies and structural analyses as well as their boundaries are indicated below. Asterisks mark residue numbering corresponding to the rat CD45 ortholog (rCD45d3d4). (**b**) Multi-angle light scattering analysis of CD45RABC (red), CD45R0 (blue) and CD45d1-d4 (violet). All constructs analysed were monomeric in solution. Measured molecular weights versus theoretical masses (dotted lines) including the contribution of glycans are: 125.0±0.5

versus 92.5 kDa for CD45RABC, 79.0±0.4 versus 68.0 kDa for CD45R0 and 64.6±0.1 versus 62.7 kDa for CD45d1-d4. (**c**) Cartoon representation of CD45d1-d4 crystal structure with individual domains colored as in (**a**). N-linked GlcNAc moieties observed in electron density maps are shown in space-filling format. (**d**) Position of disulfide bridges in the structure, identified with roman numerals; yellow spheres correspond to sulfur atoms. (**e**) Cartoon representation of individual CD45d1-d4 domains with rainbow colored β-strands (N-terminus, blue; C-terminus, red). The β3 and β4 strands are missing in d1 and truncated in d2 in the regions highlighted by ellipsoids. (**f**) Model of N-glycosylated CD45d1-d4, assuming glycosylation of every sequon. CD45d1-d4 (white) and the N-linked glycans (represented as $Man_9GlcNAc_2$ moieties; blue) are shown in surface representation. Residual GlcNAc residues observable in the electron density maps were used to position the glycans at the sites marked with asterisks.

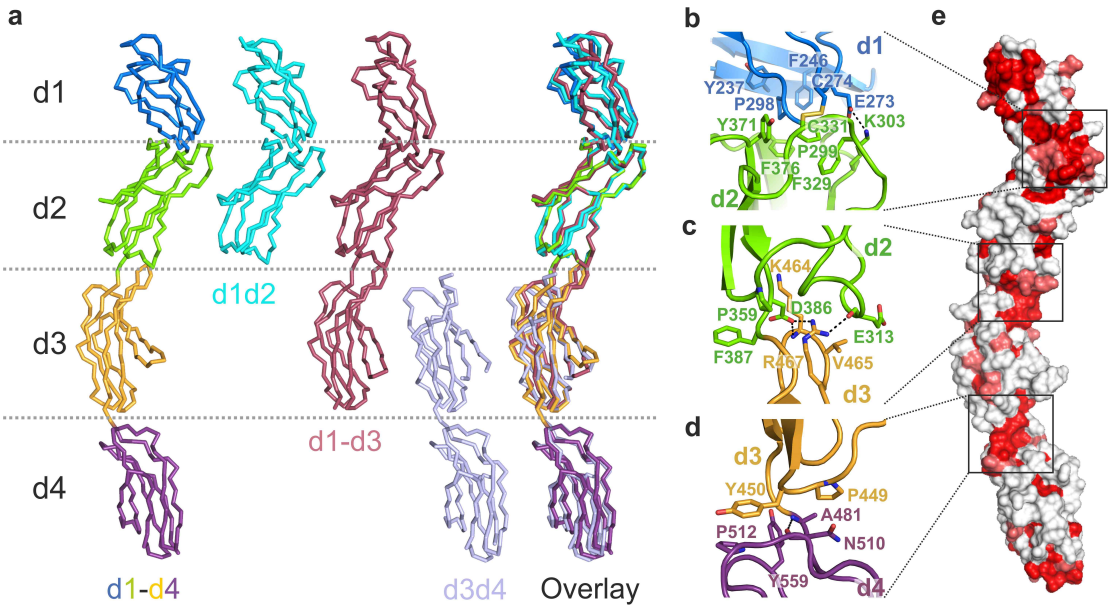

Figure 2

The human CD45 d1-d4 segment is rigid. (**a**) Comparison of the four crystal structures determined in this study. CD45d1-d4 is colored as in **Figure 1c**; CD45d1d2, cyan; CD45d1-d3, dark red; and rCD45d3d4, gray. The structures are overlaid in the right panel. (**b**-**d**) Close-up views of the inter-domain interfaces. Color coding is as in **Figure 1c**. Potential hydrogen bonds are shown as black dotted lines. Interface residues are labeled. (**e**) Surface representation of CD45d1-d4, showing the degree of conservation of surface residues based

on a structural alignment of eleven mammalian CD45 family members (data not shown). Residues are colored according to the number of identical or conservatively substituted residues at each position in the alignment: 0-6, white; 7-8, pink; and 9-11, red (see Online Methods). CD45 sequences used for the alignment were: human, UniProtKB accession number P08575; chimpanzee, H2Q0U9; gibbon, G1S8W0; rabbit, G1T2D8; dog, F1Q1U1; ferret, M3YGB4; cat, M3WN30; panda, G1M263; cow, F1MJS9; mouse, P06800; and rat, P04157).

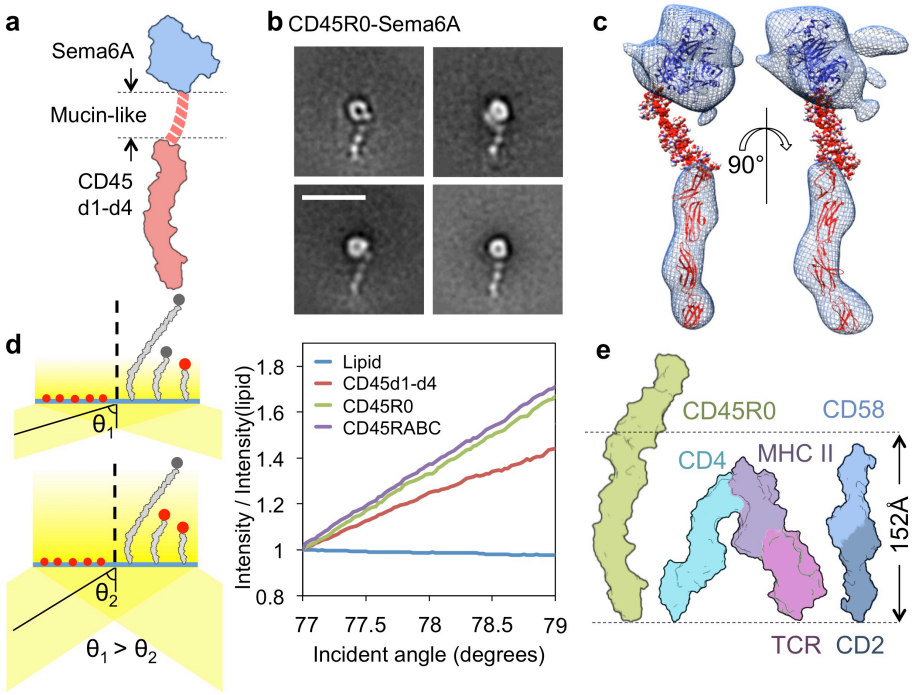

Figure 3

Axial dimensions and positioning of the CD45 ECD at a model surface. (**a**) Schematic representation of the CD45R0 ECD fused with the sema domain of Sema6A. The mucin-like sequence is drawn as a heavy dashed line. (**b**) Example class sums derived from the Sema6A-CD45R0 images obtained by negative staining electron microscopy; scale-bar is 25 nm. (**c**) Two views of a 3D reconstruction fitted with the Sema6A domain and CD45d1-d4, with the mucin-like segment modeled in between them. (**d**) Left panel, principle of VA-TIRFM. Varying the incidence angle under total internal reflection conditions changes the depth of the evanescent field illuminating the sample. This results in a change in signal, with a magnitude that depends on the distance between the fluorescent object and the surface (the molecules shown schematically are, left to right, the ECDs of CD45RABC , CD45R0 and

CD45d1-d4; red and gray circles depict fluorescing and non-fluorescing dyes). Right panel, variation in fluorescence intensity at different incidence angles for N-terminally fluorescently-labeled CD45d1-d4, CD45R0 and CD45RABC attached to an SLB, versus a fluorescent lipid in an adjacent bilayer. (**e**) Dimensions of CD45R0 versus those of a ternary CD4-TCR-MHCII complex (pdb 3T0E) and a model of the CD2-CD58 complex [using CD2d1d2 (pdb 1HNF) superimposed on the CD2-CD58 d1-d1 complex (pdb 1QA9)], based on crystal structural data and shown in surface representation (only O-linked glycans are modeled on CD45R0).

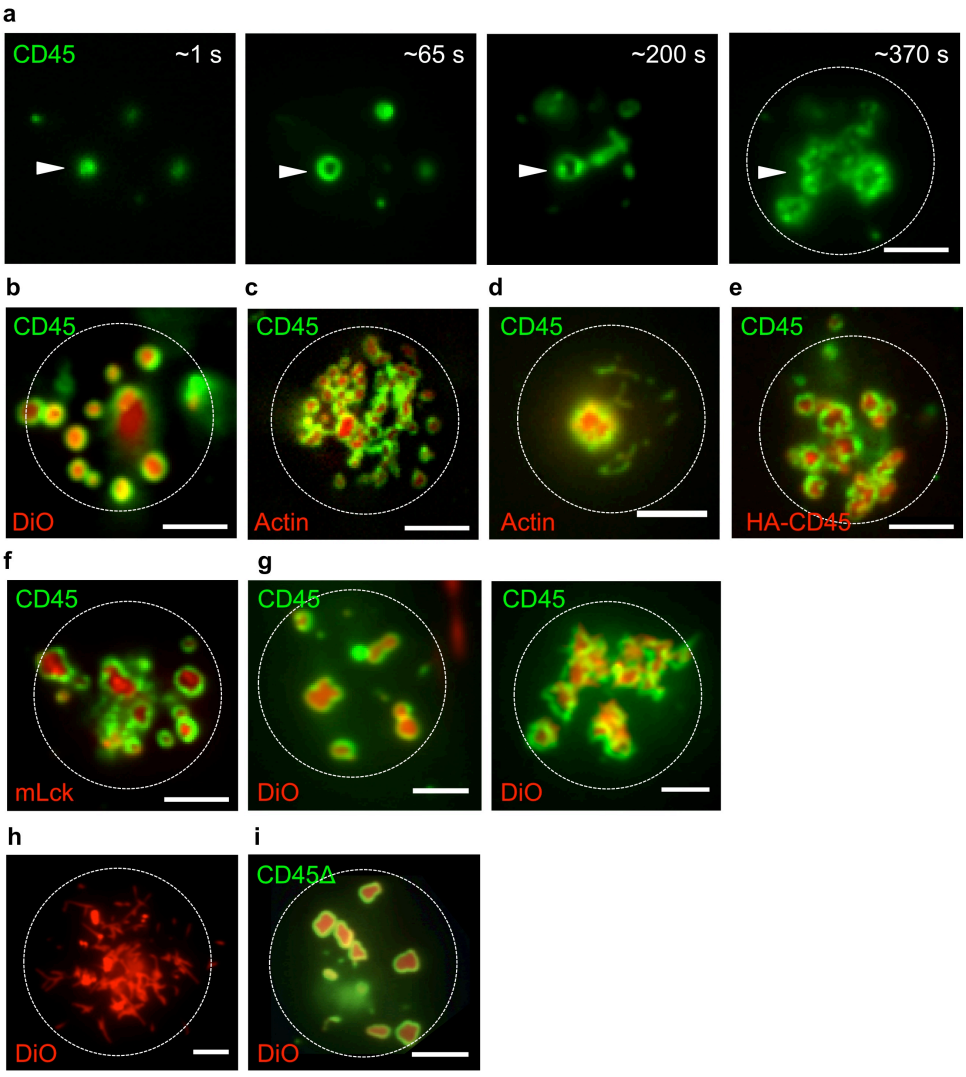

Figure 4

Close-contact formation. (**a**-**f**) CD45 (labeled with Alexa-488-tagged Fab, green) organization at contacts of Jurkat T cells with bovine IgG-coated glass imaged using TIRFM; the cell in **c** is a J.RT3-T3.5 derivative lacking TCRs. Imaging was done at 20°C. (**a**) Frames

from a time-lapse video; t = 1 s represents the time of first contact with the surface. CD45 is excluded from the contacts, which are dynamic structures that merge over time (white arrows). Distribution of CD45 (green) versus the membrane dye DiO (red; **b**), β actin labeled with mCherry (red) in the absence (**c**) and presence (**d**) of latrunculin, a truncated form of CD45 (HA-CD45) whose extracellular domain is replaced by a nine-residue HA tag (labeled with TMR via a HaloTag®, red; **e**), and mLck (labeled with TMR via a HaloTag®, red; **f**) ~120 s after contact formation. In (**g**), primary ($CD4^+$) T cells are shown interacting with IgG-coated glass with the membrane marked with DiO (red) and CD45 labeled with Alexa-488-tagged Fab (green). In (**h**) a human embryonic kidney (HEK) 293T cell, with its membrane labeled with DiO (red), is shown interacting with IgG-coated glass. In (**i**) an HEK 293T cell expressing a form of CD45RABC lacking a cytoplasmic domain (CD45Δ) is shown contacting IgG-coated glass, with the membrane marked with DiO (red) and CD45Δ labeled with Alexa-488-tagged Fab (green). White circles indicate the approximate boundary of each cell imaged in white light. Scale bars are 3 μm. The images shown are each representative of ~15 cells examined in at least three independent experiments.

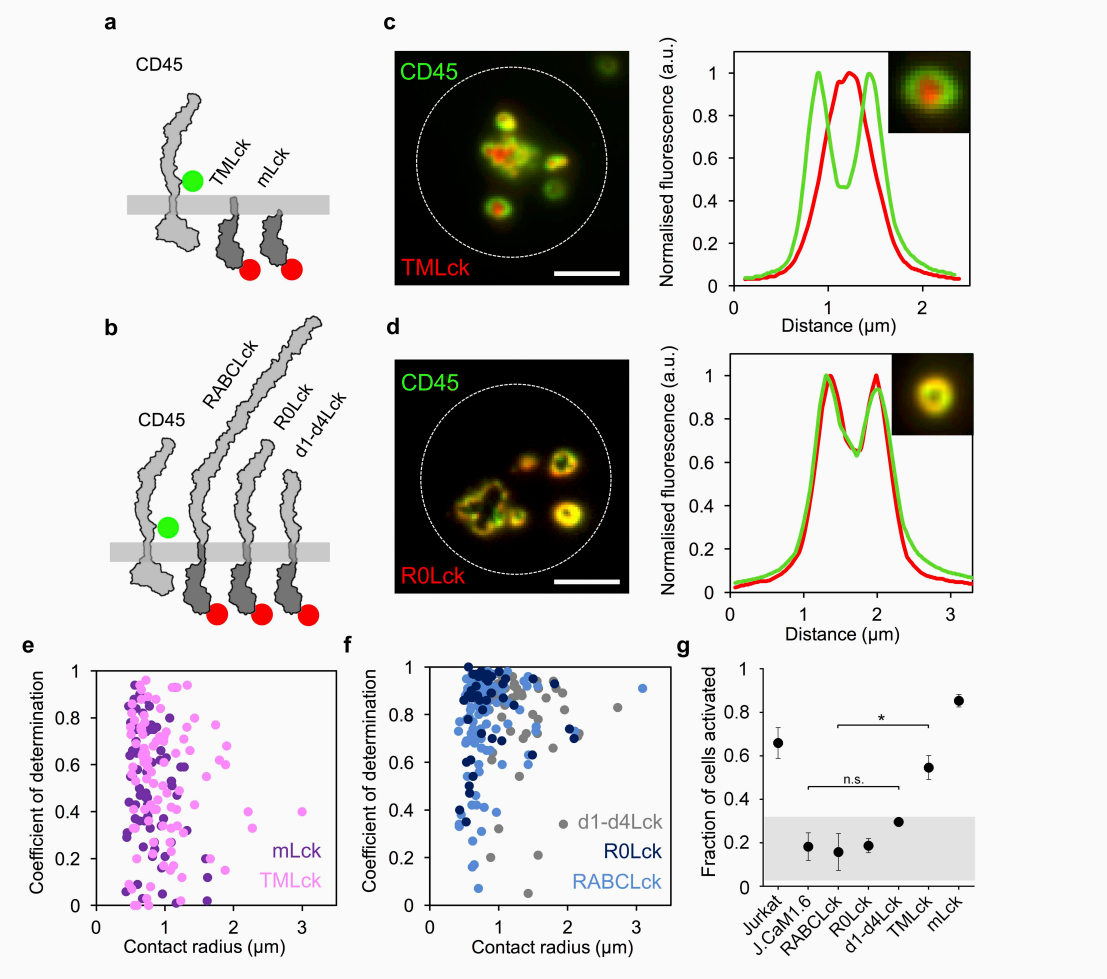

Figure 5

Large chimeric forms of Lck are excluded from and prevent signaling at close-contacts. (**a**-**d**) Comparisons of spatial organization, in Lck-deficient J.CaM1.6 T cells, of CD45 (labeled with Alexa-488-tagged Fab, green) and 'short'- or 'long'-forms of Lck (labeled with TMR via a HaloTag®, red). (**a**,**b**) Diagrams of the chimeric CD45-Lck constructs; green and red dots depict the Alexa-488 and TMR labels, respectively. (**c**) TIRFM image showing that CD45, but not short-form TMLck is excluded from the T cell-surface contacts ~120s after their formation (left), and line profile of example exclusion zone (inset: data used). (**d**) TIRFM image showing that CD45 and long-form R0Lck are equally well excluded at the contacts ~120s after their formation (left), and line profile of example exclusion zone (inset: data used). (**e**) Correlation of CD45 and Lck fluorescence (i.e. coefficient of determination) plotted as a function of the size of the contact measured for the short-form Lck molecules, i.e. mLck and TMLck, and CD45 (see Online Methods). (**f**) Correlation of CD45 and Lck fluorescence plotted as a function of the size size of the contact measured for the long-form

Lck constructs, i.e. RABCLck, R0Lck and d1-d4Lck, and CD45. Data in (**e**,**f**) were obtained from 181 cells expressing the constructs shown in (**a**,**b**); of 1096 individual contacts formed, 34% were suitable for quantitation. (**g**) Fractions of J.CaM1.6 T cells expressing the constructs depicted in (**a**,**b**) producing a calcium response upon contacting OKT3-coated glass at 20°C. Errors are standard deviations; *: all p values <0.001; n.s. p value >0.2; one-way ANOVA/posthoc Tukey comparison. The shaded part of the graph is the 95% confidence interval for the J.CaM1.6 dataset defining the range of values for individual calcium responses indistinguishable from those of the J.CaM1.6 cells. Scale bars in (**d**,**e**) are 3 µm.

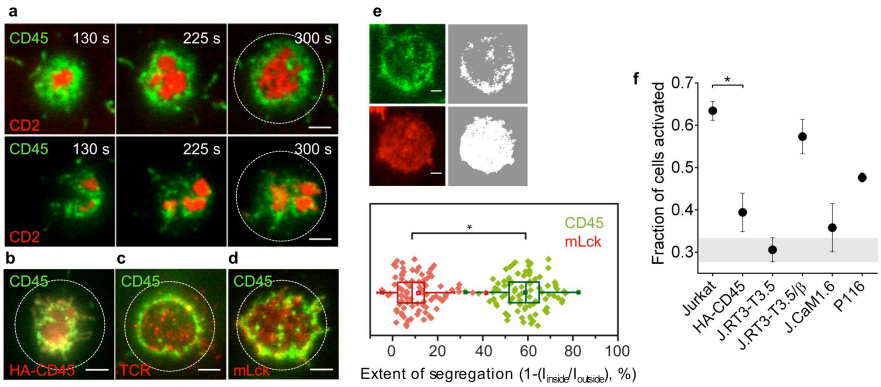

Figure 6. Ligand-independent T cell signaling on supported lipid bilayers. All measurements were undertaken at 37°C. (**a**-**d**) Size-dependent segregation of CD45 but not of TCR and mLck on rCD2-containing SLBs. The Jurkat T cells expressed T92A-mutated CD48 to initiate close-contact formation. CD45 was labeled with Alexa-488-tagged Fab (green). HA-CD45 and mLck were each labeled with TMR (red) via a HaloTag®; the TCR was labeled with TMR-tagged Fab. (**a**) Two examples of successive sets of TIRFM images taken from time-lapse videos showing the spatio-temporal organization of CD45 (green) versus rat CD2 (labeled with TMR, red) during the formation of single (top) and multi-focal (bottom) contacts. All scale bars, 2 µm. (**b**) CD45 (green) versus a truncated form of CD45 (HA-CD45, red) 44 s after contact formation. (**c**) CD45 (green) versus the TCR (red) 128 s after contact formation. (**d**) CD45 (green) and mLck (red) 580 s after contact formation. (**e**) Quantification of the spatial inhomogeneity (segregation) of CD45 and mLck distributions in the close-contacts; $^{**}P = 4\text{x}10^{-76}$, two sample t-test, unequal variance assumed, $n_{(cells)} = 85$. In the top panels binary image masks (right) used to define regions inside (gray) and outside (white) the contacts between the T cell and a SLB containing rCD2 to calculate the extent of

CD45 segregation are shown (see Online Methods). (**f**) The fraction of T cells eliciting a calcium response (detected with Fluo-4) upon contact formation. Errors are standard deviations; *P <0.001, two-tailed t-test, unequal variance assumed. The shaded part of the graph is the 95% confidence interval for the J.RT3-T3.5 dataset defining the range of values for individual calcium responses indistinguishable from those of the J.RT3-T3.5 cells.

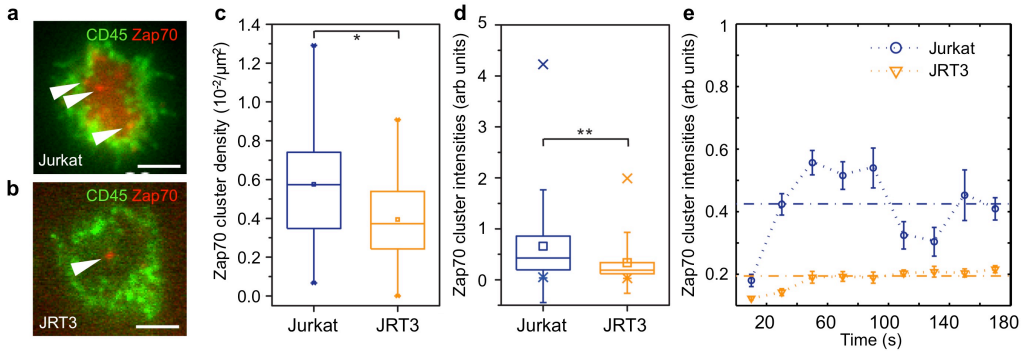

Figure 7. Zap70 recruitment to the TCR following ligand-independent signaling on supported lipid bilayers. (**a**,**b**) TIRFM images showing CD45 (labeled with Alexa-488-tagged Fab, green) and Zap70 (labeled with TMR via a HaloTag®, red) cluster accumulation at contacts 180 s post cell attachment for Jurkat (**a**) and TCR-deficient J.RT3-T3.5 (JRT3; **b**) T cells. Typical Zap70 clusters are identified with white arrows. All scale bars are 3 μm. The images shown are each representative of ~25 cells examined in at least 12 independent experiments. (**c**) Distributions of Zap70 cluster densities observed during the first 180 s of SLB contact in Jurkat and J.RT3-T3.5 T cells; *P = 0.03, Mann-Whitney-U test. (**d**) Distributions of Zap70 cluster sizes observed within the first 180 s post attachment for Jurkat and J.RT3-T3.5 T cells; **P = 7.6×10^{-81}, Mann-Whitney-U test. (**e**) Zap70 cluster size on Jurkat and J.RT3-T3.5 T cells as a function of time (20 s time bins) using cluster fluorescence intensities as an indicator of cluster size. Errors are calculated from bootstrapping. Dashed lines are medians. In all boxplots shown the central line is the median, x the mean, the edges of the box are the 25th and 75th percentiles, and the whiskers extend to the most extreme data points not considered outliers. Total numbers of cells analyzed were $n_{(Jurkat)}$ = 28 and $n_{(J.RT3\text{-}T3.5)}$ = 36; total numbers of Zap70 trajectories analyzed were $n_{(Zap70)}$ = 1794 (Jurkats) and 1311 (J.RT3-T3.5 T cells).

Online Methods

CD45 ECD constructs for crystallization and electron microscopy

For crystallization experiments fragments of the ECD of human CD45 (d1-d4, residues 223-571; d1-d3, residues 223-479; and d1d2, residues 223-392 of UniProtKB accession number P08575) were amplified from CD45RABC cDNA (a kind gift of A. Weiss) using the polymerase chain reaction (PCR). The rat CD45d3d4 fragment (residues 357-546, UniProtKB accession number P04157) was amplified from rat thymus cDNA. For the human and rat CD45 constructs, 6xhistidine tags were encoded at their 3' and 5' ends, respectively, to aid purification. The CD45d1d2 and CD45d1-d3 constructs were ligated into pHLsec vector[41] below sequence encoding the chicken RPTPσ signal peptide (cRPTPσSP). The CD45d1-d4 and rCD45d3d4 constructs were inserted into pEE14 vector[42] also below sequence encoding cRPTPσSP. For EM analysis the ECD of CD45R0 (residues 24-31, 193-575 of UniProtKB accession number P08575) was amplified from codon-optimized synthetic CD45RABC cDNA (Eurofins Genomics, Ebersberg Germany) and fused at the 5' end to the ECD of mouse Sema6A (residue 19-571 of UniProtKB accession number O35464) amplified from Sema6A cDNA (a kind gift of R. A. Robinson), using PCR. The construct, encoding Sema6A-CD45R0, was then sub-cloned into pHR vector[43] below sequence encoding cRPTPσSP.

CD45d1d2 and CD45d1-d3 were expressed transiently in 293T cells, CD45d1-d4 and rCD45d3d4 stably in Chinese hamster ovary cells, and Sema6A-CD45R0 lentivirally in 293T cells. Kifunensine added to the cultures facilitated protein deglycosylation as required[44]. Proteins were purified using metal-chelate and size-exclusion chromatography. For crystallization the proteins were also de-tagged, de-glycosylated with endoglycosidase F1 and re-purified by lectin-affinity chromatography[45]. CD45d1-d4 was twice methylated[46] for crystallization. See **Supplementary Figure 1a** for SDS-PAGE analysis of the soluble proteins.

Constructs for TIRFM imaging and signaling studies

Codon-optimized cDNA encoding ECD fragments of CD45 (RABC, residues 24-575; R0, residues 24-31 and 193-575; and d1-d4, residues 223-571) was ligated into pHLsec downstream of sequence encoding cRPTPσSP and an HA tag. DNA encoding the murine CD4 transmembrane region (residues 392-422, UniProtKB accession number P06332) was fused

with DNA encoding murine Lck (residues 1-509, UniProtKB accession number P06240) using PCR. The first residue of the kinase was replaced with lysine and Cys-20 and Cys-23 mutated to disrupt CD4 binding. The CD4-Lck construct was ligated into pHLsec vector and inserts containing the cRPTPσ-CD45-CD4-Lck constructs sub-cloned into pHR vector followed by DNA encoding HaloTag® (Promega, Southampton UK), giving RABCLck, R0Lck and d1-d4Lck. TMLck consisted of DNA encoding cRPTPσSP, an HA tag and the CD4 transmembrane and mutated Lck sequences. DNA encoding a Cys-mutated but otherwise intact Lck, called mLck, was also ligated into pHR.

HA–CD45 was generated by inserting an HA epitope after the starting methionine of mouse linker for activation (LAT; UniProtKB accession number O54957) which was spliced at Pro33 to the cytoplasmic domain of human CD45 (residues 598-1304) using a serine linker. Residue 1304 of human CD45 was then spliced to sequence encoding HaloTag®. Cell lines expressing the lentiviral constructs were generated as described[47].

Constructs for measuring CD45 length using VA-TIRFM

HaloTag® sequence was inserted into pHR below sequence encoding cRPTPσSP, followed by cDNA encoding the ECDs of CD45 (RABC, residues 24-575; R0, residues 24-31 and 193-575; and d1-d4, residues 223-571) and a 6xhistidine tag. Soluble protein expressed lentivirally in 293T cells was purified using metal-chelate and size-exclusion chromatography and then labeled using HaloLigand® TMR (Promega, Southampton UK).

Crystallization and data collection

Deglycosylated CD45 ECD samples were concentrated by ultrafiltration (CD45d1d2, 14 mg/ml; rCD45d3d4, 6.2 mg/ml; CD45d1-d3, 12 mg/ml; CD45d1-d4, 11.2 mg/ml) prior to sitting drop vapor-diffusion crystallization trials using 100 nl protein plus 100 nl reservoir. Successful crystallization conditions were: CD45d1d2 at 20.5°C in 0.1M Tris pH 8, 2.4M ammonium sulfate with 6% ethylene glycol as an additive; CD45d1-d3 at 20.5°C in 30% w/v PEG8k, 0.2M ammonium sulfate, 0.1M sodium cacodylate pH 6.5; CD45d1-d4 at 4°C in 14% w/v PEG8k, 0.2M ammonium sulfate pH 8; and rCD45d3d4 at 4°C in 10% v/v 2-propanol, 0.2M lithium sulfate, 0.1M sodium phosphate-citrate pH 4.2. For phasing, CD45d1d2 and rCD45d3d4 crystals were soaked in reservoir solution saturated with

potassium tetrachloroplatinate (9 h) and hexatantalum tetradecabromide (12 h), respectively.

X-ray diffraction data were collected at 100 K using ESRF beamlines ID23-EH1 (native and heavy atom-soaked CD45d1d2, λ = 0.9497 Å and λ = 1.0720 Å, respectively) and ID23-EH2 (native CD45d1-d3, λ = 0.8726 Å), and Diamond Light Source beamlines I03 (native rCD45d3d4, λ = 1.0714 Å), I02 (heavy atom-soaked rCD45d3d4, λ = 1.2 Å) and I04-1 (native CD45d1-d4, λ = 0.9173 Å). Data were indexed, integrated and scaled using the HKL/HKL-2000 package and xia2. See **Supplementary Table 1** for data collection statistics.

Crystal structure determination, refinement and analysis

The CD45d1d2 and rCD45d3d4 structures were determined by SAD analysis. Heavy atom positions were determined using SHELXD and solutions were input into autoSHARP for phase calculation, improvement and extension using higher resolution native data to 2.3 Å and 2.45 Å, respectively. Map quality was excellent (**Supplementary Fig. 1b-d**) allowing tracing of the complete polypeptide chains, with electron density also observable for most residual N-linked glycans (**Supplementary Fig. 1b-d**). Initial models were automatically built using ARP/wARP, followed by iterative rounds of manual model building in Coot and refinement in BUSTER, REFMAC and Phenix.

CD45d1-d3 was solved by molecular replacement using CD45d1d2 as a search model in Phaser. The model was completed by iterative rounds of manual building in Coot and refinement in BUSTER, applying target weight refinement, with the high-resolution structure of CD45d1d2 as target. CD45d1-d4 was solved using CD45d1-d3 and domain 4 of rCD45d3d4 as search models in Phaser. The model was completed by iterative rounds of manual building in Coot and refinement in REFMAC and BUSTER, applying non-crystallographic symmetry restraints. See **Supplementary Table 1** for refinement statistics and protein geometry analysis (using Molprobity). Sequence and structural alignments were performed in ClustalW and SHP, respectively; for Figure 2e conservative substitutions were defined using the following residue groupings: IV/LM/FY/NDQEBZ (single letter code). Protein interfaces were analysed using PDBePISA

(www.ebi.ac.uk/pdbe/prot_int/pistart.html). Structural figures were prepared using the PyMOL Molecular Graphics System, Version 1.6, Schrödinger, LLC.

Electron microscopy

Three microliters of 10 µg/ml Sema6A-CD45R0 was placed on a carbon-coated 300 mesh copper grid (Agar Scientific, Stansted UK) for uranyl formate staining[48]. Images were collected using an FEI T12 electron microscope operating at 80kV and nominal magnification 67,000x. Data were captured on CCD and individual particle images interactively selected using Boxer (EMAN software; see **Supplementary Figure 3a** for representative data). In total 9,079 particles were selected and subjected to image analysis in IMAGIC. After iterative centering to the sum of all images, a single round of multivariate statistical analysis and classification yielded 50 class averages. **Supplementary Figure 3b** shows all 50 class averages and corresponding "I-images". The I-images are a statistical measure of the consistency of features within class sums. Whereas in "S images" high densities correspond to the most significant image areas and are calculated as:

$$\text{S-image} = (\text{squares of the average})/(\text{average of the squares}),$$

an I-image gives the amount of information collected in the different parts of the images in bits:

$$\text{I-image} = 2\log([\text{n-1}]*\text{S-image})/(1\text{-S-image}).$$

Twenty-eight class sums were used for 3D reconstruction of Sema6A-CD45R0, also in IMAGIC, based on angular reconstitution without a reference model. The resulting 3D map was filtered to 40 Å resolution and used in iterative projection matching-based reconstruction from the raw data images in SPIDER. After five iterations the reconstruction had converged and possessed a resolution of 33 Å at FSC = 0.5 (**Supplementary Fig. 3c**). Comparison of the original class averages and reprojections of the final map were in good agreement (**Supplementary Fig. 3d**). However, whereas the densities of the CD45d1-d4 and Sema6A components were well resolved in the reconstruction no density was visible for the mucin-like segment at the contour levels shown because the map resolution was too low to resolve this feature. This is confirmed by comparison of the reconstruction fitted with Sema6A and CD45d1-d4 including a modeled, glycosylated linker (see **Fig. 3c**, main text) and density calculated for this Sema6A-CD45R0 atomic model: at 33 Å sema domain and CD45d1-d4

density clearly fit the experimental density but joining density is absent (**Supplementary Figure 3e**).

VA-TIRF microscopy

Imaging was performed using a home-built TIRF microscope (described below) modified with a kinematic mirror mount with piezoelectric adjusters (Thorlabs, Ely UK), such that the angle of incidence, and therefore field penetration depth of the output from the 561 nm laser (4 Wcm^{-2}) could be varied (above the critical angle) in objective-type TIRF. Variation in the ~77-79° range gave the greatest dynamic range for axial discrimination of the CD45 constructs. Field penetration depth was varied with a sawtooth-shaped waveform applied to the piezo amplifier (±150 V at 0.25 Hz).

Purified, histidine- and N-terminally HaloTag®-tagged CD45 constructs, i.e. CD45d1-d4, CD45R0 and CD45RABC (0.5 µg/mL in 10 mM Tris, 150 mM NaCl, pH 8.0) labeled with HaloLigand® TMR (Promega, Southampton UK; G8251) were attached to nickelated lipids in SLBs formed as described below (5 wt% 18:1 DGS-NTA(Ni), 95 wt% POPC) by incubation for 30 minutes before rinsing with buffer. VA-TIRFM signals from the proteins were compared to that from SLBs containing 0.1 wt% TRITC DHPE (N-(6-tetramethylrhodaminethiocarbamoyl)-1,2-dihexadecanoyl-sn-glycero-3-phosphoethanol-amine, triethylammonium salt; Invitrogen, Paisley UK) and 99.9 wt% POPC. Spatial variation in the TIRF excitation field intensity required normalization of sample signals against reference images corresponding to TRITC-labeled lipids in adjacent SLBs.

TIRF-intensity, I, depends on distance to the fluorophore, z, and angle of incidence, θ, according to:

$$I(z,\theta) = I_0(\theta)\exp(-z/d(\theta)) \tag{S1}$$

where d is the penetration depth (see ref. 28). Assuming collected light is proportional to I, the detected intensity from fluorophores positioned at heights h_1 and h_2 above the surface is given by:

$$I_r = \frac{\alpha I(h_1,\theta)}{I(h_2,\theta)} = \alpha\exp(-(h_1 - h_2)/d(\theta)) \tag{S2}$$

where α is a factor correcting for differences in the surface fluorophore concentration in the paired samples. Measuring the change in intensity as a function of the angle of incidence allows α to be eliminated, giving:

$$\frac{dI_r}{d\theta}\Big/ I_r = \beta(\theta)(h_1 - h_2), \text{ where } \beta(\theta) = \frac{1}{d^2(\theta)}\frac{d(d(\theta))}{d\theta} \quad \text{(S3)}$$

The average position of the fluorophore is measured in these experiments. For each protein the signal $(dI_r/d\theta)/I_r$ varied versus the labeled SLB (0.21 per degree for CD45d1-d4, 0.33 per degree for CD45R0 and 0.35 per degree for CD45RABC). From Eq. S3 the average CD45R0 and CD45RABC signals were 157% and 166% higher than for CD45d1-d4, respectively, effects we attribute to differences in the axial heights of the proteins.

SLB preparation

SLBs were prepared as described[49] with minor modifications. Glass coverslips (VWR International, Lutterworth UK) were cleaned for 1 hour in 3:1 sulfuric acid:hydrogen peroxide, followed by thorough rinsing and plasma cleaning for 15 minutes. SLBs were formed on the coverslips using press-to-seal silicone isolators (Grace Bio-Labs, Bend OR) by adsorption and subsequent rupture of lipid vesicles. The vesicles consisted of 1-palmitoyl-2-oleoyl-sn-glycero-3-phosphocholine (POPC) with either 0 or 5.0 wt% 1,2-di-(9Z-octadecenoyl)-sn-glycero-3-[(N-(5-amino-1-carboxypentyl)imino-diacetic acid)succinyl] (nickel salt) (18:1 DGS-NTA(Ni); both Avanti Polar Lipids, Alabaster USA) or 0.01 wt% Oregon Green® 488 1,2-dihexadeca-noyl-sn-glycero-3-phosphoethanolamine (OG-DHPE) in 10 mM HEPES, 150 mM NaCl, pH 7.4. Following SLB formation the vesicle solution was replaced with buffer. For experiments described in **Figs 6,7**, 0.25 μg/ml rCD2 with a H_6SRAWRHPQFGGH_6 "spacer-his" tag was bound to the SLBs.

Cell culture

Plasmid transfection and lentivirus infections were used to generate cell lines expressing the constructs described above. For imaging T cells were grown in phenol red-free RPMI supplemented with 10% FCS, 1% HEPES buffer, 1% sodium pyruvate and 1% penicillin/streptomycin ("T-cell medium").

TIRF imaging

Before imaging, T cells expressing HaloTag®-tagged proteins, i.e. mLck, TMLck, RABCLck, R0Lck, d1-d4Lck, TCRβ, HA-CD45 and Zap70 were labeled with HaloLigand® TMR for 30 minutes. The cells were then subjected to three cycles of PBS washes and 30 minute incubations in T-cell medium. Approximately 10^6 cells were then resuspended in PBS and incubated with anti-CD45 (Gap8.3) antibody Fab fragments tagged with Alexa® Fluor 488 at 22°C. Following this incubation, the cells were washed three times with PBS (involving centrifugation at 600×g, 2 minutes) and transferred to coverslips that had been cleaned with an Argon plasma (PDC-002; Harrick Plasma, Ithaca NY) and then coated with OX7 (anti-rat Thy1.1) antibody only or a 9:1 mixture of OX7 and OKT3 (anti-CD3) antibodies (total 10 µg/mL, experiments shown in **Figs 4,5**). Alternatively, the cells were allowed to settle on SLBs prepared as described above (experiments shown in **Figs 6,7**). Imaging was carried out within the first minutes following cell attachment at temperatures indicated in the figure legends.

Imaging was performed using home-built TIRF microscopes. Diode lasers operating at 488 nm (Spectra Physics, Newport, US (**Figs 4,6,7**); IBeam_488_1002; Toptica, Munich Germany (**Fig. 5**)) or 561 nm (Spectra Physics (**Figs 4,6,7**); Jive, 0561-04-01-0100-300; Cobolt, Solna Sweden (**Fig. 5**)), or a HeNe laser operating at 633 nm (Melles Griot, Rochester NY) were directed into a TIRF objective (60x Plan Apo TIRF, NA 1.45, Nikon Corporation, Tokyo Japan (**Figs 4,6,7**); N2709400, APON60XO TIRF; Olympus (**Fig. 5**)) mounted on an Eclipse TE2000-U microscope (Nikon Corporation (**Figs 4,6,7**)) or Olympus IX-71 microscope (**Fig. 5**) parallel to the optical axis and offset giving total internal reflection.

Emitted fluorescence was collected by the same objective and separated from the returning TIR beam by a dichroic (Di01-R4-5/488/561/635; Semrock, Rochester NY), split into blue and red (FF562-Di03; Semrock) components using a DV2 (Photometrics, Tuczon AZ) loaded with appropriate filters (BLP01-561R and Em01-R488-25; Semrock). Images were recorded on an EM-CCD camera (Photometrics, Roper Scientifics, Martinsried Germany, -70°C (**Figs 4,6,7**); Evolve 512, Tuczon AZ, -80°C (**Fig. 5**)) by either alternating between laser excitation sources (561 nm, ~100 Wcm^{-2} and 488 nm, 25 Wcm^{-2} as measured by

epifluorescence) using mechanical shutters (Prior Scientific, Cambridge UK) and an exposure of 400ms (**Fig. 5**), or simultaneously recording two-color fluorescence signals from 488 and 561 nm or 488 and 633 nm excitation (**Figs 4,6,7**) with each color recorded on one half of the EMCCD chip. Regularly spaced ion-beam etched holes in gold-on-glass allowed image registration with a mean alignment precision of ~120 nm. Data were acquired using single snap shots or time-lapse acquisition (**Figs 5,6,7**; exposure time 100 ms, time between frames 1-5 s) using MicroManager.

Quantitative analysis of CD45-Lck chimera segregation

Images were recorded at 33 frames per second for 400 frames, and the imaging stack averaged (mean) to give the final images. No significant changes in contact morphology were observed during this period at 20°C. Image processing techniques for automatically locating close-contacts via CD45 fluorescence proved unreliable because the exclusion zones were insufficiently uniform. Close-contacts were therefore defined "by eye" as n-sided polygons by manually tracing the CD45 (Gap 8.3 Fab) fluorescence outlining each contact in ImageJ (U. S. National Institutes of Health, Bethesda, Maryland, USA, www.imagej.nih.gov/ij).

Approximate radii were calculated for each region from its circumference and area values extracted assuming a circular distribution using:

$$radius_{polygon} = 2\frac{area_{Polygon}}{circumference_{Polygon}}$$

To quantitate CD45 and CD45-Lck chimera segregation at close-contacts (**Fig. 5e**,**f**), we measured the correlation between the CD45 and Lck images of the regions/contacts selected. Pixel intensities in the two channels were plotted against each other and a coefficient of determination (R^2) reported to a linear fit. This value was then plotted versus contact radius size (short-form constructs, **Supplementary Fig. 5a**; long-form constructs, **Supplementary Fig. 5b**). For the short-form constructs, if Lck enters the close-contacts the images will not be correlated and the linear correlation will report a small value close to 0. If long-form CD45-Lck chimeras are excluded from the close-contacts the images will correlate, giving a coefficient of determination closer to 1. The analysis will over-estimate the correlation for small contacts as revealed by the broad distribution of R^2 values for small

close-contacts (**Fig. 5e,f**). The smallest zone measurable, defined by the Abbe diffraction limit, was 174 nm agreeing with our empirically determined pixel resolution = 178 nm/pixel. The minimum observable zone of differential exclusion would have a three-pixel diameter as confirmed by the absence of measurable contacts below ~600 nm (**Fig. 5e,f**).

Calcium imaging

T cells were labeled with 4 μM Fluo-4 AM (Invitrogen, Paisley UK) for 30 minutes at 37°C and left in medium containing 2.5 mM probenecid (Invitrogen) for 20 minutes. The cells were then washed and transferred to PBS containing 2.5 mM probenecid before adding to antibody-coated slides or SLBs. A bespoke ImageJ macro detected individual cells at suitable time-points. Intensities were imported to MATLAB (R 2011b, The MathWorks, Natick, US) for further analysis. Briefly, after filtering the data with a Savitzky-Golay moving average and subtracting the average fluorescence intensity between frame 1 and the frame corresponding to the maximum fluorescence intensity, a change in fluorescence intensity above zero gave the "cell landing time". Signaling cells were identified when (i) the maximum intensity was two-fold above the intensity recorded at the landing time and (ii) "triggering time" (time of the largest subsequent fluorescence increase) > landing time. After correcting for moving cells, the landing time, triggering time and triggered proportion were reported with an error of only 8% as determined by eye for 150 randomly chosen cells.

Quantitative analysis of CD45-mLck segregation on SLBs

Bespoke MATLAB code was used to analyze the image data. First, the cell-area was manually identified using fluorescence in the 561 channel (Lck fluorescence). Binary masks were then generated corresponding to the selected cells in both the 488 and 561 channels to separate signal from background (see **Fig. 6e**): pixels were assigned a value of 1 if their intensity values I fulfilled the condition $I > (\mathrm{mean}(I_{region}) - 2 * \mathrm{std}(I_{region}))$. The binary mask created for the 488 nm (CD45 fluorescence) channel was designated to be the region of the cell surface excluded from SLB contact, and the mean intensity of the pixels corresponding to this area calculated for both the CD45 and Lck channels ($I_{outside}$). To create a binary mask describing the area of the cell corresponding to the SLB contact, the binary mask created from the CD45 channel was subtracted from the one created from the Lck channel and applied to both channels (I_{inside}). The CD45/Lck ratio in the contact was calculated from the fraction of total CD45 and Lck molecules in the contacts, i.e. $f(CD45_{tot,in}) = \frac{I_{inside}}{I_{outside}} =$

0.41 and $f\left(Lck_{tot,in}\right) = 0.88$. Assuming a 5:1 CD45 to Lck ratio outside the contact for a typical Jurkat T-cell, this means that the ratio inside changes to 5*0.41:1*0.88 (i.e. 2.3:1).

Quantitative analysis of Zap70 recruitment on SLBs

Zap70 recruitment was measured using time-lapse fluorescence image acquisition at a rate of 1 frame per second (exposure time of 500 ms). Bespoke MATLAB code was used to analyze the data. First, cell area was manually selected based on bright-field images of the cells. Corresponding images of HaloLigand®-TMR labelled Zap70 fluorescence were band-pass filtered, signals of signal molecules detected using intensity and signal-to-noise thresholds, and their positions in subsequent frames linked to form trajectories using published particle detection and tracking algorithms adapted for MATLAB (www.physics.georgetown.edu/matlab) and further modified[52]. Zap70 intensities were extracted by averaging maximum pixel intensity over multiple frames before bleaching occurred (*i.e.* before particle intensity in frame n+1 dropped below 60% of particle intensity in frame n). Intensity values were then divided by the average background fluorescence of the given cell to account for cell-to-cell variations in Zap70-Halo expression (in the presence of endogenous Zap70). For analyzing the evolution of mean particle intensity over time, the median intensity of all Zap70 trajectories observed in a time window (bin) of 20 seconds was calculated from t = 20 seconds after contact formation and the error estimated by bootstrapping (*i.e.* calculating the standard deviation of the median values of 1000 data sets created by randomly drawing samples of the size of the original data set).

Statistical methods

Data plotting and statistical analysis was performed using Origin 8.1 (OriginLab, Northampton, MA). Differences between sets of non-normally distributed data were assessed using Mann-Whitney U-tests.

References

1. van der Merwe, P. A. & Dushek, O. Mechanisms for T-cell receptor triggering. *Nat. Rev. Immunol.* **11**, 47-55 (2011).
2. Hermiston, M. L., Xu, Z. & Weiss, A. CD45: a critical regulator of signaling thresholds in immune cells. *Annu. Rev. Immunol.* **21**, 107-37 (2003).
3. Williams, A. F. & Barclay, A. N. Glycoprotein antigens of the lymphocyte surface and their purification by antibody affinity chromatography, in *Handbook of Experimental Immunology* 22.1-22.24 (Blackwell Scientific Publications, Oxford, UK, 1986).
4. Fischer, E. H., Charbonneau, H., Cool, D. E. & Tonks, N. K. Tyrosine phosphatases and their possible interplay with tyrosine kinases. *Ciba Found. Symp.* **164**, 132-40 (1992).
5. Pingel, J.T. & Thomas, M.L. Evidence that the leukocyte-common antigen is required for antigen-induced T lymphocyte proliferation. *Cell* **58**, 1055-65 (1989).
6. Secrist, J. P., Burns, L. A., Karnitz, L., Koretzky, G. A. & Abraham, R. T. Stimulatory effects of the protein tyrosine phosphatase inhibitor, pervanadate, on T-cell activation events. *J. Biol. Chem.* **268**, 5886-93 (1993).
7. Schoenborn, J. R., Tan, X. Y., Zhang, C., Shokat, K. M. & Weiss, A. Feedback circuits monitor and adjust basal Lck-dependent events in T cell receptor signaling. *Sci. Signal.* **4**, ra59 (2011).
8. Davis, S. J. & van der Merwe, P. A. The structure and ligand interactions of CD2: implications for T-cell function. *Immunol. Today.* **17**, 177-87 (1996).
9. Davis, S. J. & van der Merwe, P. A. The kinetic-segregation model: TCR triggering and beyond. *Nat. Immunol.* **7**, 803-9 (2006).
10. Springer, T. A. Adhesion receptors of the immune system. *Nature* **346**, 425-34 (1990).
11. Burroughs, N. J., Lazic, Z. & van der Merwe, P. A. Ligand detection and discrimination by spatial relocalization: A kinase-phosphatase segregation model of TCR activation. *Biophys J.* **91**, 1619-29 (2006).
12. Varma, R., Campi, G., Yokosuka, T., Saito, T. & Dustin, M.L. T cell receptor-proximal signals are sustained in peripheral microclusters and terminated in the central supramolecular activation cluster. *Immunity* **25**, 117-27 (2006).
13. Leupin, O., Zaru, R., Laroche, T., Müller, S. & Valitutti, S. Exclusion of CD45 from the T-cell receptor signaling area in antigen-stimulated T lymphocytes. *Curr. Biol.* **10**, 277-80 (2000).

14. Johnson, K.G., Bromley, S.K., Dustin, M.L. & Thomas, M.L. A supramolecular basis for CD45 tyrosine phosphatase regulation in sustained T cell activation. *Proc. Natl. Acad. Sci. USA.* **97**, 10138-43 (2000).
15. Tan, Y. X., Zikherman, J. & Weiss, A. Novel tools to dissect the dynamic regulation of TCR signaling by the kinase Csk and the phosphatase CD45. *Cold Spring Harb Symp Quant Biol.* **78**, 131-9 (2013).
16. Symons, A., Willis, A. C. & Barclay, A. N. Domain organization of the extracellular region of CD45. *Protein Eng.* **12**, 885-92 (1999).
17. Irles, C. *et al.* CD45 ectodomain controls interaction with GEMs and Lck activity for optimal TCR signaling. *Nat. Immunol.* **4**, 189-97 (2003).
18. James, J. R. & Vale, R. D. Biophysical mechanism of T-cell receptor triggering in a reconstituted system. *Nature* **487**, 64-9 (2012).
19. Choudhuri, K., Wiseman, D., Brown, M. H., Gould, K. & van der Merwe, P. A. T-cell receptor triggering is critically dependent on the dimensions of its peptide-MHC ligand. *Nature* **436**, 578-82 (2005).
20. Chakraborty, A. K. & Weiss, A. Insights into the initiation of TCR signaling. *Nat Immunol*. **15**, 798-807 (2014).
21. Barr, A. J. *et al.* Large-scale structural analysis of the classical human protein tyrosine phosphatome. *Cell* **136**, 352-63 (2009).
22. Hui, E. & Vale, R. D. In vitro membrane reconstitution of the T-cell receptor proximal signaling network. *Nat. Struct. Mol. Biol.* **21**, 133-42 (2014).
23. James, J. R. *et al.* The T cell receptor triggering apparatus is composed of monovalent or monomeric proteins. *J. Biol. Chem.* **286**, 31993-2001 (2011).
24. Aricescu, A. R. *et al.* Structure of a tyrosine phosphatase adhesive interaction reveals a spacer-clamp mechanism. *Science* **317**, 1217-20 (2007).
25. Jentoft, N. Why are proteins O-glycosylated? *Trends Biochem. Sci.* **15**, 291-4 (1990).
26. Cyster, J. G., Shotton, D. M. & Williams, A. F. The dimensions of the T lymphocyte glycoprotein leukosialin and identification of linear protein epitopes that can be modified by glycosylation. *EMBO J.* **10**, 893-902 (1991).
27. McCall, M. N., Shotton, D. M. & Barclay, A. N. Expression of soluble isoforms of rat CD45. Analysis by electron microscopy and use in epitope mapping of anti-CD45R monoclonal antibodies. *Immunology* **76**, 310-7 (1992).

28. Olveczky, B. P., Periasamy, N. & Verkman, A. S. Mapping fluorophore distributions in three dimensions by quantitative multiple angle-total internal reflection fluorescence microscopy. *Biophys. J.* **73**, 2836-47 (1997).
29. Evans, E. J. *et al.* Crystal structure and binding properties of the CD2 and CD244 (2B4)-binding protein, CD48. *J. Biol. Chem.* **281**, 29309-20 (2006).
30. Olszowy, M. W., Leuchtmann, P. L., Veillette, A. & Shaw, A. S. Comparison of p56lck and p59fyn protein expression in thymocyte subsets, peripheral T cells, NK cells, and lymphoid cell lines. *J. Immunol.* **155**, 4236-40 (1995).
31. Yokosuka, T. *et al.* Newly generated T-cell receptor microclusters initiate and sustain activation by recruitment of Zap70 and SLP-76. *Nat. Immunol.* **6**, 1253-62 (2005).
32. Coles, C. H. *et al.* Structural basis for extracellular cis and trans RPTPσ signal competition in synaptogenesis. *Nat. Commun.* **5**, 5209 (2014).
33. Garcia, K.C. *et al.* An alphabeta T cell receptor structure at 2.5 A and its orientation in the TCR-MHC complex. *Science* **274**, 209-19 (1996).
34. Garboczi, D.N. *et al.* Structure of the complex between human T-cell receptor, viral peptide and HLA-A2. *Nature* **384**, 134-41 (1996).
35. Burroughs, N. J. *et al.* Boltzmann energy-based image analysis demonstrates that extracellular domain size differences explain protein segregation at immune synapses. *PLoS Comput Biol.* **7**, e1002076 (2011).
36. van der Merwe, P.A., McNamee, P.N., Davies, E.A., Barclay, A.N. & Davis, S.J. Topology of the CD2-CD48 cell-adhesion molecule complex: implications for antigen recognition by T cells. *Curr Biol.* **5**, 74-84 (1995).
37. Parsey, M. V. & Lewis, G. K. Actin polymerization and pseudopod reorganization accompany anti-CD3-induced growth arrest in Jurkat T-cells. *J. Immunol.* **151**, 1881-93 (1993).
38. Wang, J. H. & Reinherz, E. L. The structural basis of αβ T-lineage immune recognition: TCR docking topologies, mechanotransduction, and co-receptor function. *Immunol. Rev.* **250**, 102-19 (2012).
39. Roncagalli, R. *et al.* Quantitative proteomics analysis of signalosome dynamics in primary T cells identifies the surface receptor CD6 as a Lat adaptor-independent TCR signaling hub. *Nat. Immunol.* **15**, 384-92 (2014).

40. Irving, B. A., Alt, F. W. & Killeen, N. Thymocyte development in the absence of pre-T cell receptor extracellular immunoglobulin domains. *Science* **280**, 905-8 (1998).
41. Aricescu, A. R., Lu, W. & Jones, E. Y. A time- and cost-efficient system for high-level protein production in mammalian cells. *Acta Crystallogr. D Biol. Crystallogr.* **62**, 1243-50 (2006).
42. Zufferey, R., Nagy, D., Mandel, R. J., Naldini, L. & Trono, D. Multiply attenuated lentiviral vector achieves efficient gene delivery in vivo. *Nat. Biotechnol.* **15**, 871-5 (1997).
43. Cockett, M. I., Bebbington, C. R. & Yarranton, G. T. High level expression of tissue inhibitor of metalloproteinases in Chinese hamster ovary cells using glutamine synthetase gene amplification. *Biotechnology* **8**, 662-667 (1990).
44. Chang, V. T. *et al.* Glycoprotein structural genomics: solving the glycosylation problem. *Structure* **15**, 267-73 (2007).
45. Davis, S. J. *et al.* Ligand binding by the immunoglobulin superfamily recognition molecule CD2 is glycosylation-independent. *J. Biol. Chem.* **270**, 369-75 (1995).
46. Walter, T. S. *et al.* Lysine methylation as a routine rescue strategy for protein crystallization. *Structure* **14**, 1617-22 (2006).
47. Dunne, P. D., Fernandes, R. A., McColl, J., Yoon, J. W., James, J. R., Davis, S. J. & Klenerman, D. DySCo: Quantitating associations of membrane proteins using two-color single-molecule tracking. *Biophys. J.* **97**, L5-L7 (2009).
48. Ohi, M., Li, Y., Cheng, Y. & Walz, T. Negative staining and image classification – powerful tools in modern electron microscopy. *Biol. Proced. Online* **6**, 23-34 (2004).
49. Jönsson, P. *et al.* Hydrodynamic trapping of molecules in lipid bilayers. *Proc. Natl. Acad. Sci. U. S. A.* **109**, 10328-33 (2012).
50. Crocker, J. C. & Grier, D. G. When like charges attract: the effects of geometrical confinement on long-range colloidal interactions. *Phys. Rev. Lett.* **77**, 1897-1900 (1996).